# Electronic Structure of $Al_3O_n$ and $Al_3O_n^-$ ($n = 1-3$) Clusters

**Ana Martínez and Francisco J. Tenorio**

*Instituto de Investigaciones en Materiales, Universidad Nacional Autónoma de México, Ciudad Universitaria, Circuito Exterior, A. P. 70-360, Delegación de Coyoacán, 04510 México D. F., México*

**J. V. Ortiz***

*Department of Chemistry, Kansas State University, Manhattan, Kansas 66506-3701*

*Received: May 9, 2001; In Final Form: June 15, 2001*

Density functional, quadratic configuration interaction and electron propagator calculations have yielded structures, isomerization energies, and anion vertical electron detachment energies pertaining to $Al_3O_n^-$ and $Al_3O_n$, where $n = 1$, 2, or 3. These data suffice for an accurate assignment of recent anion photoelectron spectra. Peaks whose relative intensities vary with experimental conditions of ion preparation and transport are associated with isomers whose energies are close to those of the lowest singlet structures. Dyson orbitals associated with the lowest electron detachment energies are dominated by Al-centered functions with antibonding relationships to nearby O centers.

## Introduction

Oxides of aluminum occur in a variety of ceramics, minerals, reactive surfaces and catalytic supports. Combustion and oxidation of aluminum lead to the creation of many intermediates whose structure and reactivity stimulate intense study. Aluminum-rich species are especially pertinent to interfaces between bulk $Al_2O_3$ and metallic Al phases.

$Al_3O$ has been identified in the gas phase as a product of reactions between Al clusters and oxygen.[1,2] Hartree−Fock and perturbative calculations on $Al_3O$ encountered a $^2B_2$, T-shaped minimum and a $^2A_1$, Y-shaped transition state within 1 kcal/mol of each other.[3] In the latter study, possible multiconfigurational character was noted as a possible hazard and relationships to Jahn−Teller distortions from a $D_{3h}$ structure were broached. Subsequent investigations on $Al_3O$ and other hypermetallic molecules concentrated on ionization energies and electron propagator methods were employed for this purpose.[4]

Photoelectron spectra of $Al_3O_n^-$ clusters, where $n = 0-5$, were presented by Wang's group at several photon energies.[5] These workers investigated the sequential oxidation behavior of anion electron detachment energies and found that, as $n$ increases, electron affinities of the neutral clusters grow. With changes in ion source and carrier gas conditions, the relative intensities of prominent spectral features change. This effect implies the presence of more than one isomer in each mass-selected, anion photoelectron spectrum.

A detailed examination of $Al_3O$ and $Al_3O^-$ potential energy surfaces near the $D_{3h}$ structure considered the importance of strong correlation effects pertaining to Jahn−Teller distortions.[6] Wave functions at $C_{2v}$ minima for $^2B_2$ $Al_3O$ and $^1A_1$ $Al_3O^-$ each were dominated by a single configuration. A $D_{3h}$ $^3A_2'$ structure for $Al_3O^-$ lay higher than the singlet. To interpret anion photoelectron spectra, configuration interaction (CI) calculations were performed on $Al_3O$ at both anionic structures. The lowest electron detachment energies of the $C_{2v}$ and $D_{3h}$ isomers were ascribed to the two lowest peaks at 1.68 and 1.22 eV, respectively, in the experimental spectrum. Doublet excitation energies inferred from CI state energies were compared with spectral features at higher electron binding energies.

A subsequent study with similar computational procedures considered $Al_3O_2$, $Al_3O_2^-$, $Al_3O_3$, and $Al_3O_3^-$.[7] For each anion, two isomers were very close in energy. Doublet excitation energies inferred from CI calculations were compared to splittings of photoelectron peaks.

In this paper, we attempt to assign the most prominent peaks in the photoelectron spectra of $Al_3O^-$, $Al_3O_2^-$, and $Al_3O_3^-$ and to account for the changes in their relative intensities with respect to the conditions under which the anions are produced. Density functional methods suffice for identification of likely structures of the anions and to confirm the similarity of neutral structures in their ground states. After refinement of the anion structures with quadratic configuration interaction methods, various electron propagator approximations are used to determine vertical electron detachment energies. These results are compared to photoelectron data and to previous calculations.

## Methods

**Density Functional Calculations.** All calculations have been carried out using the program GAUSSIAN-98.[8] Full geometry optimization without symmetry constraints was performed using the hybrid B3LYP density functional (DF)[9] and the 6-311+G(2d) basis.[10] Full geometry optimizations starting from several initial geometries have been performed to locate distinct minima on potential energy surfaces. In search of the global minimum, several multiplicities and initial structures were considered. We cannot exclude the possibility that global minima were missed, but the diversity of initial geometries and spin multiplicities that were examined is sufficient to inspire confidence that the global minimum has been identified. Optimized geometries were verified with frequency calculations.

**Electron Propagator Calculations.** The most stable anionic structures from DF calculations were reexamined with additional geometry optimizations at the QCISD level.[11] 6-311G(D) or

---

* To whom correspondence should be addressed. E-mail: ortiz@ksu.edu.

10.1021/jp011763r CCC: $20.00

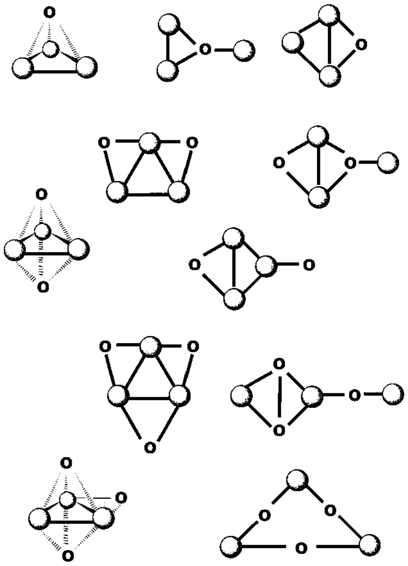

**Figure 1.** Initial structures in geometry optimizations.

larger basis sets with more polarization functions were used.[10] Only minor discrepancies between DF and QCISD structures were found.

QCISD geometries were used in subsequent electron propagator[12] calculations of the vertical electron detachment energies (VEDEs) of the anions. 6-311+G(2df) and 6-311+G(3d2f) basis sets were used.[10]

To each VEDE calculated with the electron propagator, there corresponds a Dyson spin–orbital

$$\phi^{\mathrm{Dyson}}(x_1) = \sqrt{N}\int \psi_{\mathrm{anion}}(x_1, x_2, x_3, ..., x_N) \times \psi_{\mathrm{neutral}}(x_2, x_3, x_4, ..., x_N)\,\mathrm{d}x_2\,\mathrm{d}x_3\,\mathrm{d}x_4 ...\,\mathrm{d}x_N \quad (1)$$

whose normalization integral equals the pole strength $p$ where

$$p = \int |\phi^{\mathrm{Dyson}}(x_1)|^2 \mathrm{d}x_1 \quad (2)$$

In the zeroth-order electron propagator, ionization energies are given by Koopmans's theorem, Dyson orbitals equal canonical Hartree–Fock (HF) orbitals, and pole strengths equal unity. In the present, correlated calculations, however, Dyson orbitals are linear combinations of HF orbitals and pole strengths lie between 1 and 0. Since the Dyson orbitals are subject to a nonlocal, energy-dependent potential known as the self-energy, relaxation, and correlation corrections to ionization energies and pole strengths are present. Plots of Dyson orbitals are generated with MOLDEN.[13]

Two approximations in electron propagator theory are used here. The NR2 method is suitable for calculating the lowest electron detachment energies of closed-shell species.[14] For ionization energies of typical closed-shell molecules below 20 eV, the average absolute error is less than 0.2 eV. If a molecule is suspected of having significant biradical character, or if an anion has a concentrated negative charge distribution, the BD-T1 method may be employed.[15] Here, a Brueckner doubles, coupled-cluster reference state is adopted and the full set of couplings among simple field operators and triple field operator products (except for 2ph–2hp couplings) is calculated.

## Results and Discussion

**Density Functional Geometry Optimization.** The initial geometries that were used are shown in Figure 1. We tested different bond distances and angles for each structure. For neutral and anionic $Al_3O$, $Al_3O_2$, and $Al_3O_3$, several stationary points on each potential energy surface were found. Figures 2–4 present the most stable (neutral and anionic) structures for $Al_3O$, $Al_3O_2$, and $Al_3O_3$, respectively.

For $Al_3O$, there are two stable structures, with an energy difference of 14.5 kcal/mol. For the anionic system, the structures pertain to different spin multiplicities (singlet and triplet). The ground state is a singlet and resembles structures obtained in previous studies.[3,6] The singlet–triplet splitting is 3.2 kcal/mol and there is also another triplet at 7.8 kcal/mol above the singlet.

For the $Al_3O_2$ system, two different $C_{2v}$ minima are shown in Figure 3. The energy difference between the neutral structures is 11.6 kcal/mol. For the ground state, there are no Al–Al bonds. It seems that the dissociation of the aluminum trimer stabilizes the system. For the anionic case, there are two structures with similar stability. Both are singlets and the energy difference between them is 0.4 kcal/mol. This energy difference is very small and we cannot say with certainty whether one structure is more stable than the other. The triplet planar structure is 28.0 kcal/mol higher in energy. For $Al_3O_2$ and $Al_3O_2^-$, there are stable $D_{3h}$ structures which lie at 37.3 and 22.8 kcal/mol, respectively, above the minima. Planar structures are preferred over three-dimensional ones.

The present structures for $Al_3O_2$ and $Al_3O_2^-$ are in good agreement with those obtained using another basis.[7] In the latter work, the energy difference between the kite and chain anions is −0.4 kcal/mol. For $Al_3O_2$, the separation between the two lowest structures is 12.2 kcal/mol.

For $Al_3O_3$, two $C_{2v}$ minima are shown in Figure 4. The energy difference between the neutral structures is 11.5 kcal/mol. For the ground state, there is only one Al–Al bond. For the anionic system, there are two structures with similar stability. Both are singlets and the energy difference between them is 0.7 kcal/mol. This energy difference is very small and we cannot predict which structure is more stable. The triplet planar structure is 15.4 kcal/mol higher in energy. For $Al_3O_3$ and $Al_3O_3^-$, there are stable three-dimensional structures which lie at 52.4 and 45.4 kcal/mol, respectively, above the respective, global minima. Once again, planar structures are preferred over three-dimensional ones.

In another DFT study of $Al_3O_3$ and $Al_3O_3^-$, the relative energies of the two lowest doublets and singlets are 11.1 and 0.9 kcal/mol, respectively.[7] These data and the structures that accompany them are in good agreement with the present results.

## Ab Initio Results

**$Al_3O^-$.** For $Al_3O^-$, the lowest $C_{2v}$ singlet ($^1A_1$) and the two lowest triplet ($^3B_1$ and $^3A_2$) structures found in the DF calculations were reoptimized at the QCISD/6-311G(2df) level. Whereas the singlet structure is lower than the $^3B_1$ form by 3.2 kcal/mol in DF optimizations, the present QCISD energy difference is 4.5 kcal/mol (0.19 eV). Discrepancies between DF and QCISD bond lengths are 0.02 Å or less; QCISD values are slightly smaller. Optimizations on the $^3A'_2$ anion with $D_{3h}$ symmetry produced a total energy that is 0.20 eV above the lower $C_{2v}$ triplet.

In the photoelectron spectrum of $Al_3O^-$,[5] peaks occur at 1.22 (X′), 1.68 (X), 3.0 (A), 3.5 (B), 4.2 (C), and 5.0 (D) eV. The intensity of the X′ feature is enhanced by hotter conditions in the anion source.

BD-T1/6-311+G(3d2f) results on the singlet at 1.20, 3.39, 3.86, and 5.03 eV correspond to $^2B_2$, $^2A_1$, $^2B_2$, and $^2A_1$ final

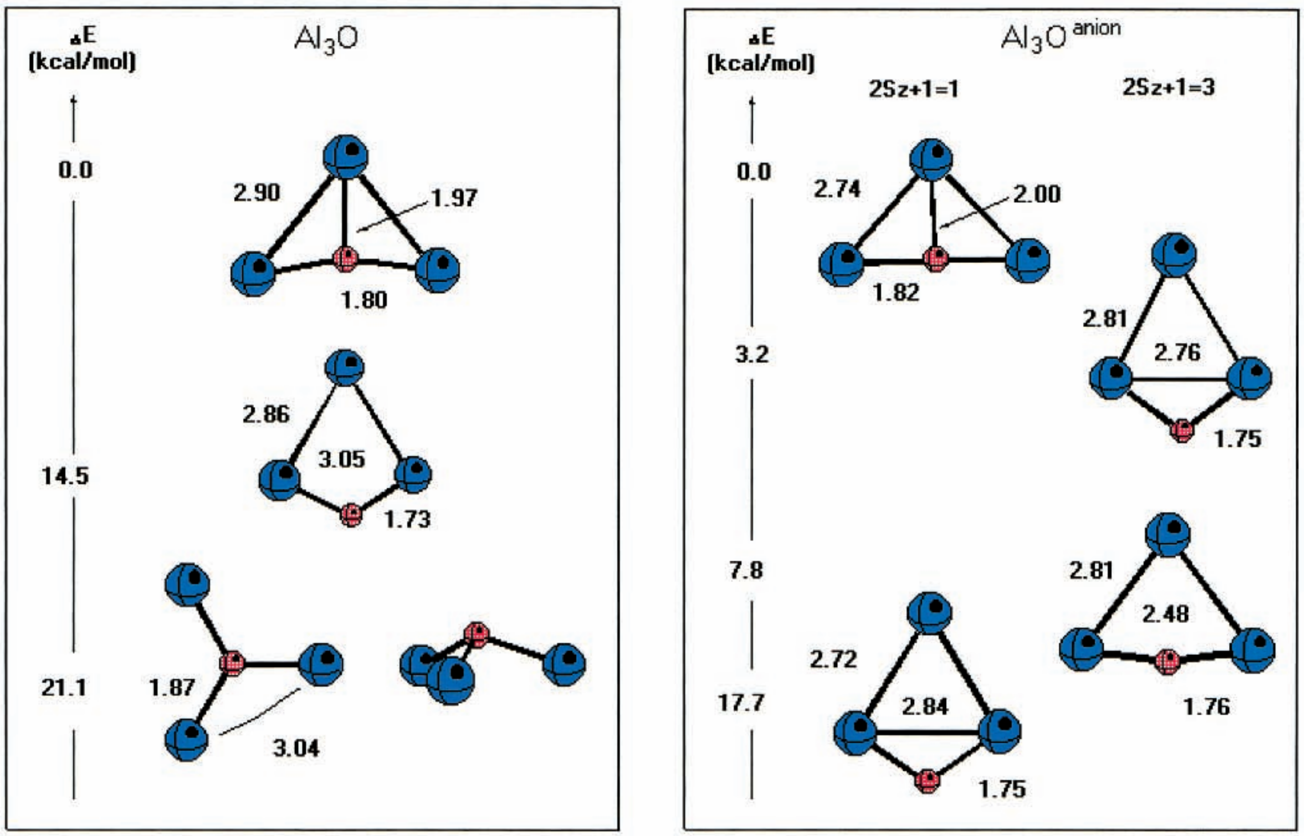

**Figure 2.** $Al_3O$ and $Al_3O^-$ structures and energies.

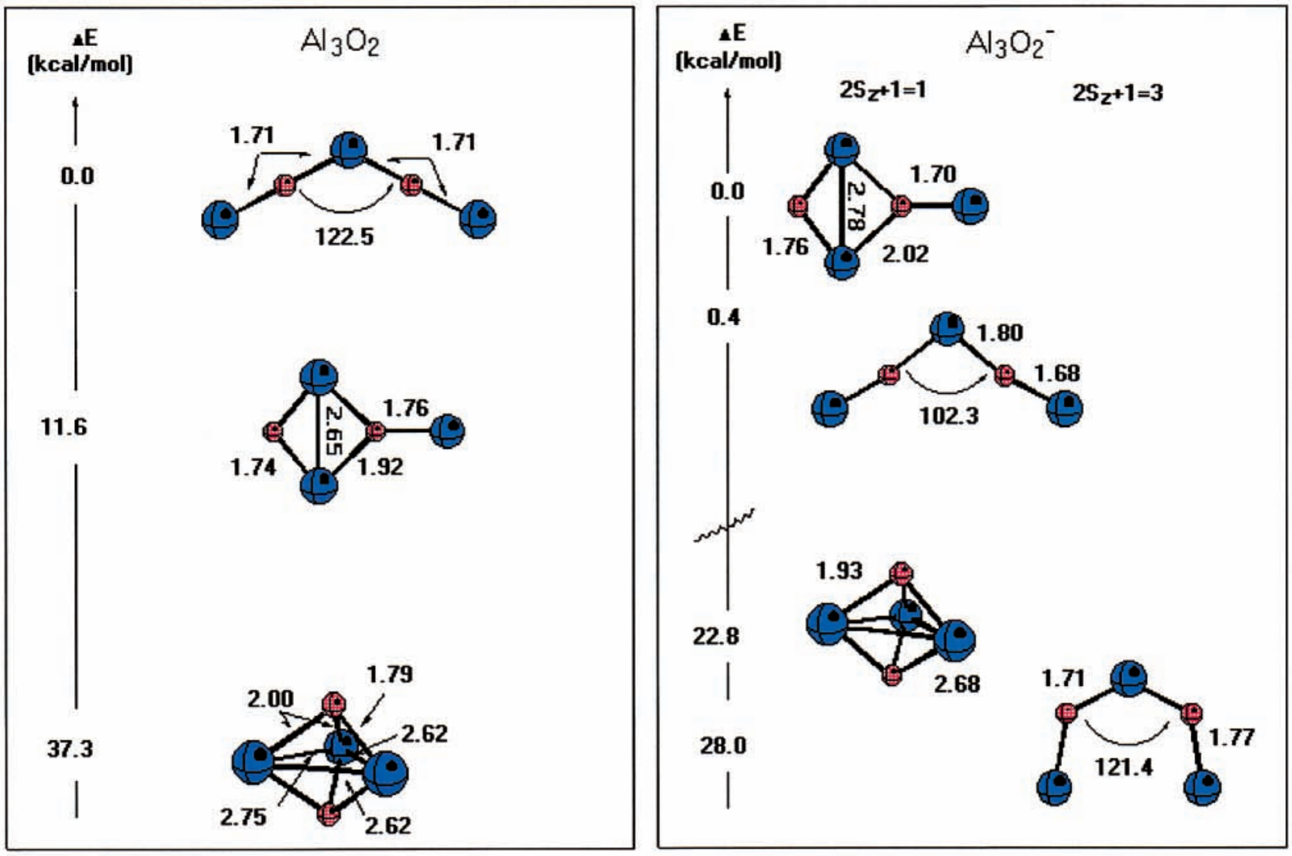

**Figure 3.** $Al_3O_2$ and $Al_3O_2^-$ structures and energies.

states of $Al_3O$, respectively. (Table 1.) These states may be assigned to the X′, B, C, and D peaks. The low pole strength of the last calculated VEDE indicates that there are nearby states with the same symmetry label. In the photoelectron spectrum,

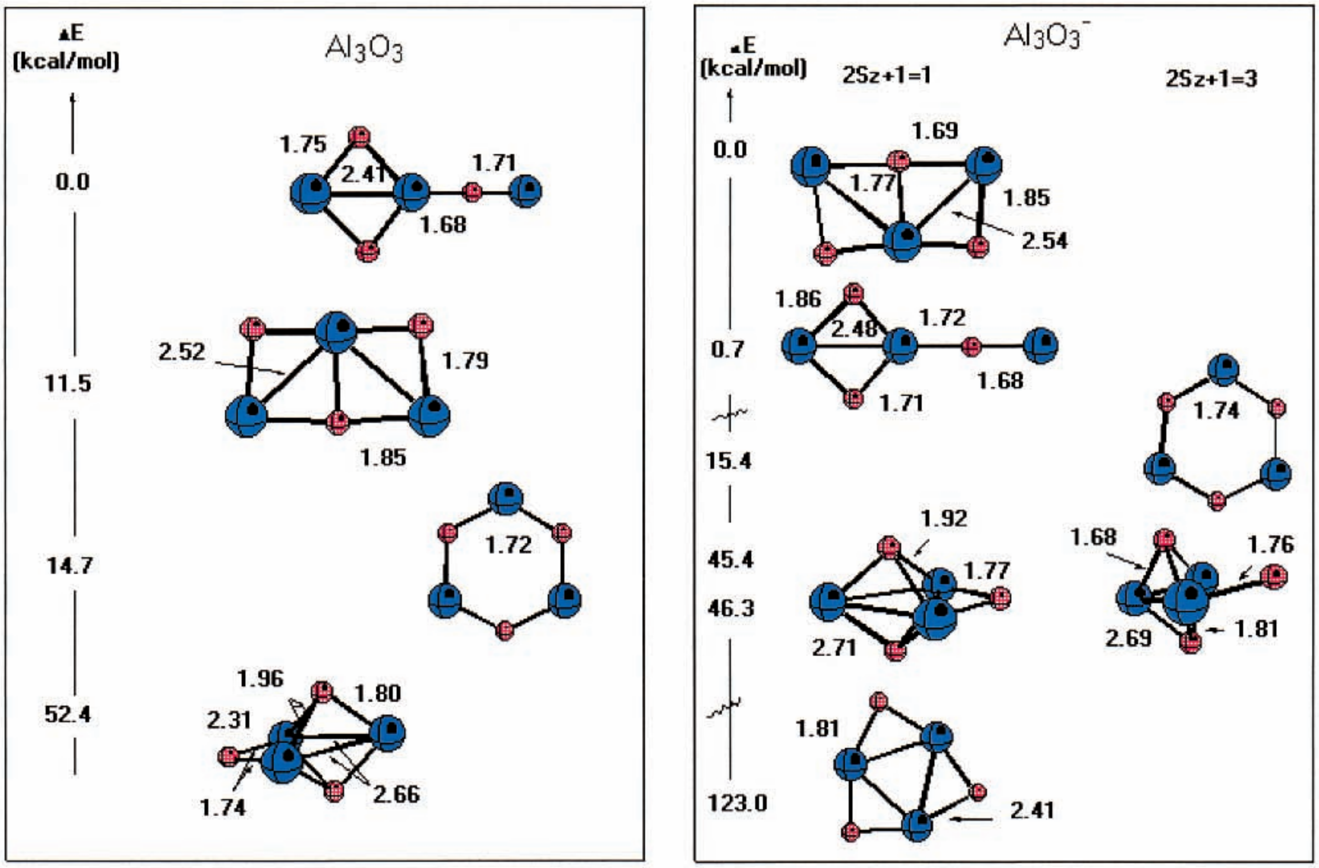

**Figure 4.** $Al_3O_3$ and $Al_3O_3^-$ structures and energies.

**TABLE 1: $Al_3O^-$ VEDEs (eV)**

| initial state (energy)[a] | final state | BD-T1[b] (*p*)[c] | BD-T1[d] (*p*)[c] | ΔQCISD(T)[e] | PES[f] |
|---|---|---|---|---|---|
| $^1A_1$<br>(0.0) | $^2B_2$ | 1.20<br>(0.87) | 1.16<br>(0.87) | | 1.22 X′ |
| | $^2A_1$ | 3.39<br>(0.82) | 3.34<br>(0.82) | | 3.5 B |
| | $^2B_2$ | 3.86<br>(0.80) | 3.81<br>(0.80) | | 4.2 C |
| | $^2A_1$ | 5.03<br>(0.42) | 4.99<br>(0.45) | | 5.0 D |
| $^3B_1$<br>(0.19) | $^2A_1$ | | | 1.55 | 1.68 X |
| | $^2B_1$ | | | 1.67 | 1.68 X |
| | $^4B_1$ | | | 2.94 | 3.0 A |
| $^3A_2$<br>(0.39) | $^2B_2$ | | | 1.00 | 1.22 X′ |
| | $^2B_1$ | | | 1.57 | 1.68 X |
| | $^4A_2$ | | | 3.27 | 3.5 B |

[a] QCISD/6-311G(2df) relative energies of anions. [b] BD-T1/6-311+G(3d2f) VEDEs. [c] Pole strengths. [d] BD-T1/6-311+G(2df) VEDEs. [e] QCISD(T)/6-311+G(2df) VEDEs. [f] Anion photoelectron spectra.[5]

the D peak has many features that are spread over a wide energy range (±0.4 eV). When these calculations are repeated with the 6-311+G(2df) basis, the results are essentially the same: 1.16, 3.34, 3.81, and 4.99 eV. (This basis therefore will be used for calculations on larger clusters.) Calculations with equation-of-motion, coupled-cluster methods obtain similar results for the first three states.[16]

ΔQCISD(T) VEDEs were calculated with the 6-311+G(2df) basis for the $^3B_1$ anionic structure obtained at the QCISD/6-311G(2df) level. $^2A_1$, $^2B_1$, and $^4B_1$ final states at 1.55, 1.67, and 2.94 eV correspond closely to experimental peaks X and A. The near coincidence of the first two states explains the larger intensity of the X feature.

Results for the $^3A_2$ anion coincide somewhat less with experiment. Under hot ion source conditions, electron detachment from this anion to the $^2B_2$ final state may contribute to the increased intensity of the X′ peak. The $^2B_1$ and $^4A_2$ final states are predicted to contribute to the X and B features.

The Dyson orbital (Figure 5a) for the singlet's first VEDE contains Al−Al bonding lobes that explain the increases in these bond lengths in $Al_3O$. For the next three VEDEs (Figure 5b−d), the Dyson orbitals consist chiefly of Al-centered hybrids with large s character. Small oxygen contributions display an antibonding relationship with neighboring Al functions. These results confirm simple electron counting rules based on a dianionic oxygen that leaves eight valence electrons for the aluminums.

According to this reasoning, the $^3B_1$ state consists of $O^{2-}$ coordinated to $Al_3^+$. All unrestricted Hartree−Fock orbitals pertaining to the three final states of Table 1 are Al-centered. The orbital for this triplet's lowest VEDE (Figure 5e) has a $\pi$ node in the nuclear plane. For the $^3B_1$ to $^2B_1$ transition, the orbital (Figure 5f) consists chiefly of Al 3p functions with large lobes on the exterior of the cluster. For the $^4B_1$ case, the orbital (Figure 5g) bears a close resemblance to its counterpart for the second VEDE of the singlet anion.

For $Al_3O^-$, six of the eight Al-centered electrons may be assigned to combinations of 3s-like hybrids. The two remaining electrons are assigned to multicentered, bonding orbitals.

**$Al_3O_2^-$.** For $Al_3O_2^-$, the two lowest $C_{2v}$ singlet structures were reoptimized at the QCISD/6-311G(d) level. The QCISD energy difference is 3.6 kcal/mol (0.16 eV) and it exceeds the DF value by 3.2 kcal/mol. Discrepancies between DF and QCISD bond lengths are 0.02 Å or less.

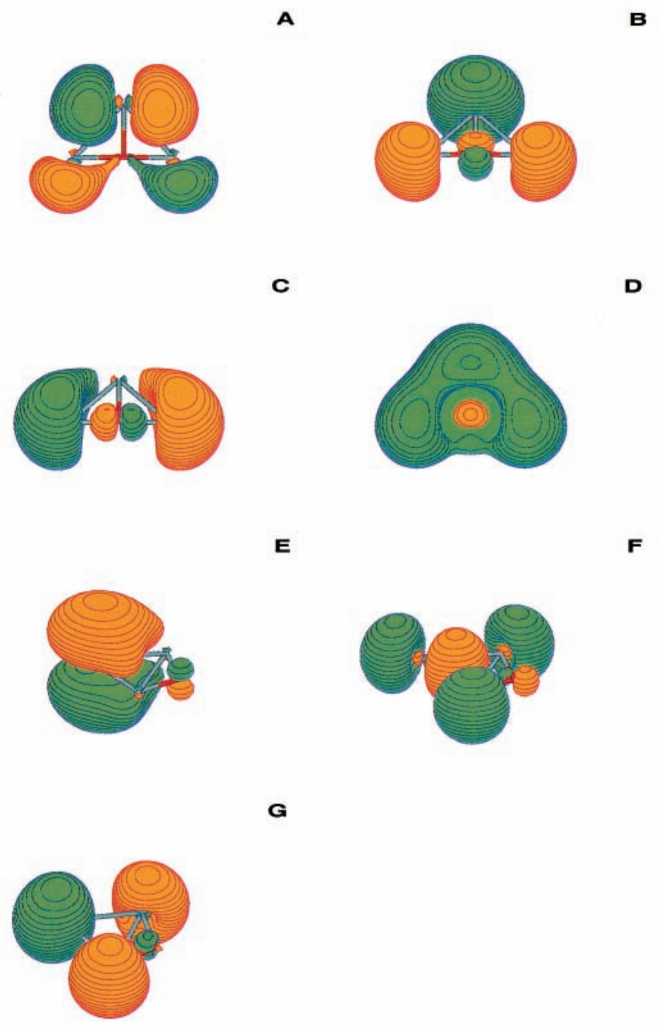

**Figure 5.** Dyson orbitals for VEDEs of $Al_3O^-$: (a) $^1A_1 \rightarrow {}^2B_2$, (b) $^1A_1 \rightarrow {}^2A_1$, (c) $^1A_1 \rightarrow {}^2B_2$, (d) $^1A_1 \rightarrow {}^2A_1$, (e) $^3B_1 \rightarrow {}^2A_1$, (f) $^3B_1 \rightarrow {}^2B_1$, (g) $^3B_1 \rightarrow {}^4B_1$.

In the photoelectron spectrum of $Al_3O_2^-$,[5] intense peaks occur at 2.29 (X), 3.5 (A) and 5.1 (C) eV. Less intense features lie at 1.8 (X′) and 4.7 (B) eV. The intensity of the X′ feature depends on the conditions of the anion source. When the spectrum is taken with pure He carrier gas instead of a mixture with a low concentration of $O_2$, the relative intensity of the X′ peak is reduced, but not completely eliminated. Because these observations were made with 355 nm radiation, no information on the effects of the carrier gas on the A, B, or C peaks is available.

NR2 and BD-T1 results with the 6-311+G(2df) basis indicate that the X and A peaks may be assigned respectively to $^2B_2$ and $^2A_1$ final states of the kite form. (Table 2.) NR2 and BD-T1 predictions also bracket the position of the C peak. These three VEDEs have large pole strengths, especially in the BD-T1 approximation. BD-T1 results are within 0.2 eV of each experimental value. Similar results have been obtained with equation-of-motion, coupled-cluster calculations.[16]

Propagator calculations also show that the less stable chain form has VEDEs that correspond to $^2A_1$ and $^2B_2$ final states. NR2 and BD-T1 values bracket the positions of the X′ and B peaks. Predictions on the second $^2A_1$ final state coincide with less intense features that lie between the B and C peaks.

**TABLE 2: $Al_3O_2^-$ VEDEs (eV)**

| geometry (energy)[a] | final state | NR2[b] (p)[c] | BD-T1[d] (p)[c] | PES[e] |
|---|---|---|---|---|
| kite<br>(0.0) | $^2B_2$ | 2.06<br>(0.88) | 2.38<br>(0.89) | 2.29 X |
| | $^2A_1$ | 3.18<br>(0.86) | 3.55<br>(0.88) | 3.5 A |
| | $^2A_1$ | 5.06<br>(0.81) | 5.31<br>(0.88) | 5.1 C |
| | $^2B_1$ | 5.75<br>(0.80) | 6.04<br>(0.85) | |
| chain<br>(0.16) | $^2A_1$ | 1.60<br>(0.87) | 2.06<br>(0.88) | 1.8 X′ |
| | $^2B_2$ | 4.56<br>(0.78) | 4.83<br>(0.89) | 4.7 B |
| | $^2A_1$ | 4.83<br>(0.82) | 5.15<br>(0.88) | |
| | $^2B_2$ | 6.04<br>(0.81) | 6.36<br>(0.85) | |

[a] QCISD/6-311G(d) relative energies of anions. [b] NR2/6-311+G(2df) VEDEs. [c] Pole strengths. [d] BD-T1/6-311+G(2df) VEDEs. [e] Anion photoelectron spectra.[5]

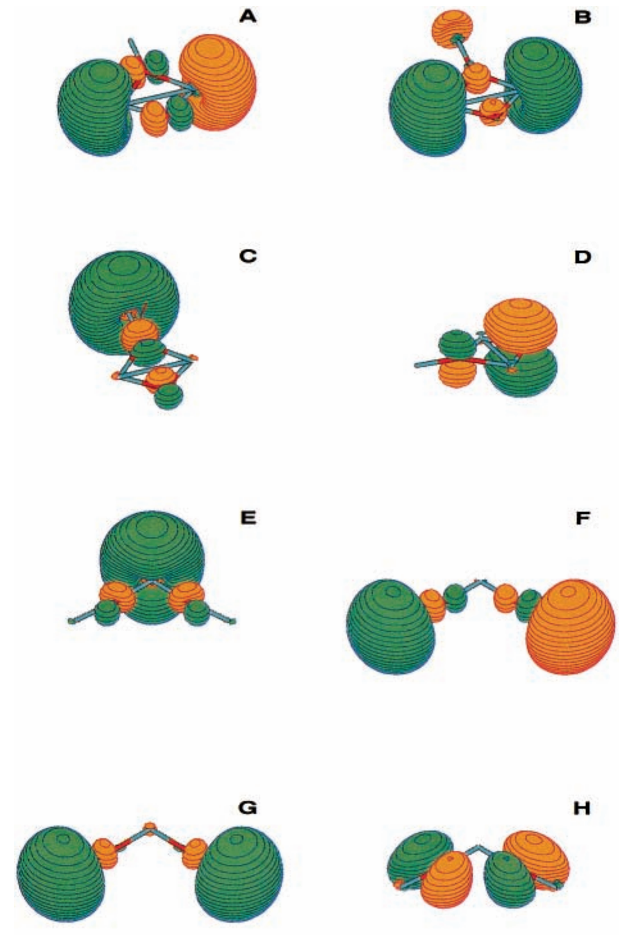

**Figure 6.** Dyson orbitals for VEDEs of $Al_3O_2^-$: (a) kite $^1A_1 \rightarrow {}^2B_2$, (b) kite $^1A_1 \rightarrow {}^2A_1$, (c) kite $^1A_1 \rightarrow {}^2A_1$, (d) kite $^1A_1 \rightarrow {}^2B_1$, (e) chain $^1A_1 \rightarrow {}^2A_1$, (f) chain $^1A_1 \rightarrow {}^2B_2$, (g) chain $^1A_1 \rightarrow {}^2A_1$, (h) chain $^1A_1 \rightarrow {}^2B_2$.

Dyson orbitals (Figure 6a−b) for the first two VEDEs of the kite form consist chiefly of nonbonding lobes on the ring Al atoms. These lobes have opposite phases for the $^2B_2$ final state and significant O p orbital participation that creates Al−O antibonding relationships. In the other case ($^2A_1$ final state), the ring Al lobes have identical phases and the remaining atoms have s contributions that also produce antibonding relationships with the ring Al atoms. For the third VEDE (another $^2A_1$ final state) of the kite form, the Dyson orbital (Figure 6c) exhibits large nonbonding lobes on the nonring Al. Antibonding

**TABLE 3: $Al_3O_3^-$ VEDEs (eV)**

| geometry (energy)[a] | final state | NR2[b] (*p*)[c] | BD-T1[d] (*p*)[c] | PES[e] |
|---|---|---|---|---|
| box<br>(0.0) | $^2B_2$ | 2.72<br>(0.88) | 3.07<br>(0.89) | 2.96 X |
| | $^2A_1$ | 3.36<br>(0.88) | 3.73<br>(0.89) | 3.7 A |
| kite<br>(0.20) | $^2A_1$ | 1.94<br>(0.88) | 2.36<br>(0.89) | 2.25 X′ |
| | $^2B_2$ | 5.19<br>(0.90) | 5.37<br>(0.87) | 5.2 B |
| | $^2A_2$ | 5.20<br>(0.84) | 5.46<br>(0.86) | 5.2 B |
| | $^2A_1$ | 5.88<br>(0.87) | 6.15<br>(0.90) | |

[a] QCISD/6-311G(d) relative energies of anions. [b] NR2/6-311+G(2df) VEDEs. [c] Pole strengths; [d]BD-T1/6-311+G(2df) VEDEs. [e] Anion photoelectron spectra.[5]

relationships involving O p functions are seen here. In the Dyson orbital (Figure 6d) for the fourth VEDE, the most important contribution is made by O p orbitals that are perpendicular to the nuclear plane, especially on the two-coordinate center. An antibonding relationship with the three-coordinate O p orbital obtains.

In the chain form, the Dyson orbital (Figure 6e) corresponding to the lowest VEDE ($^2A_1$ final state) is dominated by a nonbonding lobe on the central Al. Minor, antibonding contributions from O p functions are present as well. In contrast, the central Al makes little contribution to the Dyson orbital (Figure 6f) corresponding to the second VEDE, where the final state is $^2B_2$. Instead, large nonbonding lobes with opposite phases appear on the terminal Al atoms. Here again, there are antibonding O p contributions. In the Dyson orbital (Figure 6g) for the third VEDE, the same functions appear, but with phase relationships set by the final state's $^2A_1$ symmetry. For the fourth Dyson orbital (Figure 6h), the largest contributions come from O p functions in the nuclear plane that are perpendicular to nearby bond axes and that have opposite phases.

A simple pattern of localization applies to both isomers. By counting both O atoms as dianions, the Al atoms are left with six electrons which are distributed in the Al-dominated Dyson orbitals that correspond to the three lowest VEDEs. Higher VEDEs therefore pertain to Dyson orbitals that consist chiefly of O functions.

**$Al_3O_3^-$.** After the two lowest $C_{2v}$ singlet structures were reoptimized at the QCISD/6-311G(d) level, the box structure is lower than the kite by 4.6 kcal/mol (0.20 eV) instead of 0.7 kcal/mol with DF energies. DF and QCISD bond lengths agree to within 0.01 Å of each other.

In the photoelectron spectrum of $Al_3O_3^-$, intense peaks occur at 2.96 (X) and 3.7 (A) eV. Less intense features lie at 2.25 (X′) and 5.2 (B) eV. The intensity of the X′ feature is enhanced with higher laser fluence. This effect was attributed to photoisomerization.

NR2 and BD-T1 results with the 6-311+G(2df) basis indicate that the X and A peaks may be assigned to $^2B_2$ and $^2A_1$ final states of the box form of $Al_3O_3$, respectively. (Table 3.) NR2 and BD-T1 values bracket the experimental peaks. Equation-of-motion, coupled-cluster calculations arrive at similar conclusions.[16]

Propagator calculations also show that the less stable kite form has three VEDEs that correspond to $^2A_1$, $^2B_2$ and $^2A_2$ final states, respectively. NR2 and BD-T1 predictions are close to the X′ peak. The $^2B_2$ and $^2A_2$ predictions correspond to the highly structured B feature.

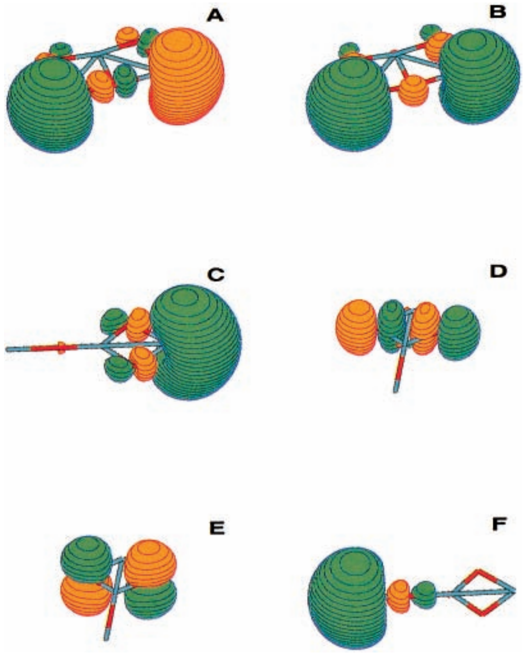

**Figure 7.** Dyson orbitals for VEDEs of $Al_3O_3^-$: (a) box $^1A_1 \rightarrow {}^2B_2$, (b) box $^1A_1 \rightarrow {}^2A_1$, (c) kite $^1A_1 \rightarrow {}^2A_1$, (d) kite $^1A_1 \rightarrow {}^2B_2$, (e) kite $^1A_1 \rightarrow {}^2A_2$, (f) kite $^1A_1 \rightarrow {}^2A_1$.

For the box form, the Dyson orbital (Figure 7a) for the lowest VEDE ($^2B_2$ final state) is built principally from nonbonding lobes on corner Al atoms with opposite phases. Antibonding interactions with O p functions are present as well. In the Dyson orbital (Figure 7b) for the next VEDE ($^2A_1$ final state), the same atomic contributions are present, but with symmetric phase relationships across one of the symmetry planes.

In the kite form, the Dyson orbital (Figure 7c) for the lowest VEDE ($^2A_1$ final state) consists mostly of a nonbonding lobe on the two-coordinate Al atom. Small antibonding contributions from ring O p functions are present also. An antibonding relationship between in-plane p functions of the ring O atoms obtains for the Dyson orbital (Figure 7d) belonging to the $^2B_2$ final state. For the $^2A_2$ final state, the Dyson orbital (Figure 7e) is an antibonding combination of ring O p orbitals that are perpendicular to the nuclear plane. For the fourth VEDE, the Dyson orbital (Figure 7f) is concentrated on the terminal Al atom. Here, a nonbonding lobe is delocalized slightly into the neighboring O p function with an antibonding phase relationship. Unlike the box form, the second Al-localized Dyson orbital pertains to the fourth VEDE in the kite structure.

After counting eight electrons for each oxygen dianion, four valence electrons remain for the aluminums. These electrons are described by two Al-centered Dyson orbitals in each isomer.

## Conclusions

Density functional optimizations have produced $C_{2v}$ structures for doublet $Al_3O$ and for singlet and triplet $Al_3O^-$. Very little energy separates the $^1A_1$ and $^3B_1$ states in their optimum geometries. Subsequent QCISD optimizations confirm these results and indicate that the $D_{3h}$ form of triplet $Al_3O^-$ is less stable than the two lowest $C_{2v}$ forms. Electron propagator and QCISD(T) results for the VEDEs of the singlet and the lowest triplet are in close agreement with anion photoelectron spectra without the employment of any empirical factors and provide an explanation for the relative intensities of the most prominent peaks. For the singlet and triplet anions, six electrons correspond to orbitals that are chiefly combinations of Al 3s functions. The last two electrons are assigned to multicenter, bonding orbitals.

A similar computational strategy leads to kite and chain structures for $Al_3O_2^-$ which are very close in energy. QCISD optimizations reinforce this conclusion. For $Al_3O_2$, there are two similar structures, but the chain form is clearly lower in energy. Combination of electron propagator results for the two isomers provides an excellent account of the anion photoelectron spectrum. The X′ feature corresponds to the less stable chain anion. For the three lowest VEDEs, there are Dyson orbitals with dominant contributions from 3s-like Al hybrids and minor, antibonding admixtures of 2p functions on oxygens.

Density functional and QCISD results agree that box and kite isomers of $Al_3O_3^-$ are the third case where there are two structures with nearly identical energies. After removal of an electron, the kite form is energetically preferred. The union of electron propagator VEDE predictions for the two isomers gives an excellent description of the $Al_3O_3^-$ photoelectron spectrum. The less stable kite isomer is responsible for the X′ feature. In the kite form, the two lowest VEDEs correspond to Al-centered Dyson orbitals. However, in the box form, two Al-centered Dyson orbitals belong to the first and fourth VEDEs, while oxygen-centered functions dominate the second and third Dyson orbitals.

**Acknowledgment.** This work was supported by the National Science Foundation under grant CHE-9873897, by the Kansas DEPSCoR program, by CONACyT and DGAPA, UNAM. Dirección General de Computo Académico at UNAM is acknowledged for providing computer time. Mrs. Sara Jiménez Cortés is acknowledged for her work with the references. Dr. Olga Dolgounitcheva assisted with the generation of Figures 5−7. We thank Dr. Marcel Nooijen of Princeton University for a preprint of ref 16.

## References and Notes

(1) Cox, D. M.; Trevor, D. J.; Whetten, R. L.; Rohlfing, E. A.; Kaldor, A. *J. Chem. Phys.* **1986**, *84*, 4651.

(2) Jarrold, M. F.; Bower, J. E. *J. Chem. Phys.* **1987**, *87*, 5728.

(3) Boldyrev, A. I.; Schleyer, P. v. R. *J. Am. Chem. Soc.* **1991**, *113*, 9045.

(4) Zakrzewski, V. G.; von Niessen, W.; Boldyrev, A. I.; Schleyer, P. v. R. *Chem. Phys. Lett.* **1993**, *174*, 167.

(5) Wu, H.; Li, X.; Wang, X.-B.; Ding, C.-F.; Wang, L.-S. *J. Chem. Phys.* **1998**, *109*, 449.

(6) Ghanty, T. K.; Davidson, E. R. *J. Phys. Chem. A* **1999**, *103*, 2867.

(7) Ghanty, T. K.; Davidson, E. R. *J. Phys. Chem. A* **1999**, *103*, 8985.

(8) Frisch, M. J.; Trucks, G. W.; Schlegel, H. B.; Scuseria, G. E.; Robb, M. A.; Cheeseman, J. R.; Zakrzewski, V. G.; Montgomery, J. A., Jr.; Stratmann, R. E.; Burant, J. C.; Dapprich, S.; Millam, J. M.; Daniels, A. D.; Kudin, K. N.; Strain, M. C.; Farkas, O.; Tomasi, J.; Barone, V.; Cossi, M.; Cammi, R.; Mennucci, B.; Pomelli, C.; Adamo, C.; Clifford, S.; Ochterski, J.; Petersson, G. A.; Ayala, P. Y.; Cui, Q.; Morokuma, K.; Malick, D. K.; Rabuck, A. D.; Raghavachari, K.; Foresman, J. B.; Cioslowski, J.; Ortiz, J. V.; Stefanov, B. B.; Liu, G.; Liashenko, A.; Piskorz, P.; Komaromi, I.; Gomperts, R.; Martin, R. L.; Fox, D. J.; Keith, T.; Al-Laham, M. A.; Peng, C. Y.; Nanayakkara, A.; Gonzalez, C.; Challacombe, M.; Gill, P. M. W.; Johnson, B. G.; Chen, W.; Wong, M. W.; Andres, J. L.; Head-Gordon, M.; Replogle, E. S.; Pople, J. A. *Gaussian 98*, revision A8; Gaussian, Inc.: Pittsburgh, PA, 1998.

(9) (a) Becke, A. D. *J. Chem. Phys.* **1993**, *98*, 5648. (b) Lee, C.; Yang, W.; Parr, R. G. *Phys. Rev. B* **1988**, *37*, 785.

(10) (a) Krishnan, R.; Binkley, J. S.; Seeger, R.; Pople, J. A. *J. Chem. Phys.* **1980**, *72*, 650. (b) Clark, T.; Chandrasekhar, J.; Spitznagel, G. W.; Schleyer, P. v. R. *J. Comput. Chem.* **1983**, *4*, 294. (c) Frisch, M. J.; Pople, J. A.; Binkley, J. S. *J. Chem. Phys.* **1984**, *80*, 3265. (d) McLean, A. D.; Chandler, G. S. *J. Chem. Phys.* **1980**, *72*, 5639.

(11) Pople, J. A.; Head-Gordon, M.; Raghavachari, K. *J. Chem. Phys.* **1987**, *87*, 5968.

(12) (a) Ortiz, J. V. In *Computational Chemistry: Reviews of Current Trends*; Leszczynski, J., Ed.; World Scientific: Singapore, 1997; Vol. 2, p 1. (b) Ortiz, J. V. *Adv. Quantum Chem.* **1999**, *35*, 33. (c) Ortiz, J. V.; Zakrzewski, V. G.; Dolgounitcheva, O. In *Conceptual Trends in Quantum Chemistry*; Kryachko, E. S., Ed.; Kluwer: Dordrecht, 1997; Vol. 3, p 465.

(13) Schaftenaar, G. MOLDEN 3.4, CAOS/CAMM Center, The Netherlands, 1998.

(14) Ortiz, J. V. *J. Chem. Phys.* **1998**, *108*, 1008.

(15) (a) Ortiz, J. V. *Chem. Phys. Lett.* **1998**, *296*, 494. (b) Ortiz, J. V. *Chem. Phys. Lett.* **1998**, *297*, 193.

(16) Nayak, S. K.; Nooijen, M. Private communication.